

Globular clusters in ORBIT: Complete dynamical characterisation of the Milky Way globular cluster population through updated orbital reconstruction

M. De Leo^{1,2,3,4,*} , M. Zoccali^{3,4} , J. Olivares-Carvajal^{3,4} , B. Acosta-Tripailao^{3,4},
F. Gran⁵ , and R. Contreras-Ramos^{3,4} 

¹ Dipartimento di Fisica e Astronomia, Università degli Studi di Bologna, Via Piero Gobetti 93/2, Bologna 40129, Italy

² Osservatorio di Astrofisica e Scienza dello Spazio di Bologna, INAF, Via Piero Gobetti 93/3, Bologna 40129, Italy

³ Instituto de Astrofísica, Pontificia Universidad Católica de Chile, Av. Vicuña Mackenna 4860, 782-0436 Macul, Santiago, Chile

⁴ Instituto Milenio de Astrofísica MAS, Av. Vicuña Mackenna 4860, 782-0436 Macul, Santiago, Chile

⁵ Université Côte d'Azur, Observatoire de la Côte d'Azur, CNRS, Laboratoire Lagrange, 06304 Nice, France

Received 3 July 2025 / Accepted 2 December 2025

ABSTRACT

Context. In hierarchical structure formation, the content of a galaxy is determined both by its in-situ processes and by material added via accretions. Globular clusters, in particular, represent a window into the study of the different merger events that a galaxy has undergone. Establishing the correct classification of in-situ and accreted tracers, and distinguishing the various progenitors that contributed to the accreted population are important tools to deepen our understanding of galactic formation and evolution.

Aims. This study aims to refine our knowledge of the Milky Way's assembly history by examining the dynamics of its globular cluster population and establishing an updated classification among in-situ objects and the different merger events identified.

Methods. We used a custom-built orbit integrator to derive precise orbital parameters, integrals of motions and adiabatic invariants for the globular cluster sample studied. By properly accounting for the rotating bar, which transforms the underlying model into a time-varying potential, we performed a complete dynamical characterisation of the globular clusters.

Results. We present a new catalogue of clear associations between globular clusters and structures (both in-situ and accreted) in the Milky Way, along with a full table of derived parameters. Using all available dynamical information, we attributed previously unassociated or misclassified globular clusters to different progenitors, including those responsible for the Aleph, Antaeus, Cetus, Elqui, and Typhon merger events.

Conclusions. Using a custom-built orbit integrator and properly accounting for the time-varying nature of the Milky Way potential, we demonstrate the depth of information that can be extracted from a purely dynamical analysis of the Galaxy's globular clusters. Merging our dynamical analysis with complementary chronochemical studies, will allow us to uncover the remaining secrets of the accretion history of the Milky Way.

Key words. methods: numerical – celestial mechanics – Galaxy: formation – globular clusters: general – Galaxy: kinematics and dynamics – Galaxy: structure

1. Introduction

In the prevailing paradigm of Λ Cold Dark Matter (Λ CDM) the structure of the Universe is believed to have formed hierarchically (Peebles 1965; Peebles & Yu 1970), with the largest overdensities accreting smaller neighbours and becoming the present-day massive galaxies (White & Rees 1978; Read et al. 2006). This turbulent process leaves traces that can be studied and decoded in the stellar and globular cluster (GC) populations of the final surviving galaxy, which allow the identification of the properties and contribution of the populations formed in-situ and of the accreted material from the mergers (Eggen et al. 1962; Searle & Zinn 1978; Bullock & Johnston 2005). Our Galaxy, the Milky Way (MW), provides a privileged window through which we can study the processes shaping galactic formation and evolution by analysing its stellar and GC populations. Due to the complexities of stellar and cluster formation, GCs offer a better opportunity to study the merger history and accreted

content of a galaxy (e.g. Belokurov & Kravtsov 2024, and references therein). To this end, it is of paramount importance to discriminate between in-situ and accreted GCs. Initial studies aimed at distinguishing the two families used available chemical and spatial information (Zinn 1985, 1996). Later, the availability of more accurate chemical data and age estimations enabled the use of age-metallicity relations (AMR, Marín-Franch et al. 2009; Forbes & Bridges 2010; Leaman et al. 2013). Running in parallel with chronochemical techniques, the availability of samples with complete position and velocity information allowed the use of integrals of motions (IoMs) and adiabatic invariants (such as the actions), which are conserved after mergers, to isolate substructures in dynamical parameter spaces (Helmi & White 1999; Helmi & de Zeeuw 2000; Binney & Tremaine 2008; Gómez et al. 2010). Concurrently, the accreted family was further divided with more detailed identifications of the first confirmed mergers, Sagittarius (Ibata et al. 1994) and the so-called “Helmi Streams” (Helmi et al. 1999). The floodgates of discovery opened with the data releases from the *Gaia* mission (Gaia Collaboration 2016), which provided position and

* Corresponding author: micheled189@gmail.com

velocity information for millions of targets, and with complementary wide spectroscopic surveys (chief among them the Apache Point Observatory Galactic Evolution Experiment, APOGEE, [Majewski et al. 2017](#)). These data led to the identification of several candidate merger events, a research that is still ongoing due to the continuous discovery of new structures. The seminal work of [Massari et al. \(2019\)](#) initiated systematic efforts to classify merger events, characterise them in various parameter spaces, and establish affiliations between the MW GCs and different progenitors. Refined research techniques using clustering algorithms ([Lövdal et al. 2022](#); [Ruiz-Lara et al. 2022](#); [Dodd et al. 2023](#)) enabled the identification of numerous new substructures. Robust spectroscopic and photometric analyses allow increasingly precise estimations of the age and chemical composition of stars and GCs ([Horta et al. 2023](#); [Massari et al. 2023](#); [Ceccarelli et al. 2024](#)) facilitating the establishment of links with their progenitors. One often-overlooked piece of the puzzle is the potential model used to derive the orbital parameters, the IoMs, and the adiabatic invariants. To properly capture the inherent intricacies of the structure of the MW it is necessary to incorporate all observed components of the Galaxy. In particular, the rotating bar is crucial both for the direct effect it has on the inner regions of the MW and for the time-varying nature of its action, which creates resonances ([Chiba et al. 2021](#); [Chiba & Schönrich 2021](#); [Trick 2022](#); [Dillamore et al. 2024](#)). We developed the ORBITAL INTEGRATION TOOL (ORBIT) as a flexible, transparent, and efficient code to perform orbit integrations with static and time-varying MW potentials. ORBIT was used in [Olivares Carvajal et al. \(2024\)](#) to study the RR Lyrae bulge population, and this paper presents our first results on MW GCs. This work is a stepping stone towards a deeper understanding of how perturbations and time-varying components of MW potentials shape and affect the inventory and structure of our Galaxy.

In Section 2, we present the data catalogues used in this work, Section 3 contains an in-depth description of ORBIT and the underlying potential model it uses, Section 4 presents our results, which we discuss in Section 5, while Section 6 provides a summary of our conclusions.

2. Data

The main source of the data used in this work is the extensive repository of GC parameters compiled by Baumgardt et al.¹ ([Baumgardt 2017](#); [Baumgardt & Hilker 2018](#); [Baumgardt & Vasiliev 2021](#); [Vasiliev & Baumgardt 2021](#)). For all GCs in the Gran “family” we use the Multi Unit Spectroscopic Explorer (MUSE, [Stuik et al. 2006](#); [Bacon et al. 2010](#); [Ströbele et al. 2012](#); [Hartke et al. 2020](#)) radial velocities reported by [Gran et al. \(2024\)](#) in place of those reported in the Baumgardt repository. We do the same with VVV-CL001, using the radial velocity from MUSE data reported in [Olivares Carvajal et al. \(2022\)](#). Likewise, for Patchick 126 and VVV-CL160, we use the proper motions and radial velocities measured with a combination of Gaia DR3 ([Gaia Collaboration 2023](#)), Vista Variables in the Via Lactea eXtended survey (VVV-X, [Minniti et al. 2010](#); [Saito et al. 2012](#)), and Immersion GRating INfrared Spectrometer (IGRINS, [Park et al. 2014](#); [Mace et al. 2018](#)) by [Garro et al. \(2023\)](#). Finally, we complemented the sample with a few additions from more recent works: VVV-CL002 ([Moni Bidin et al. 2011](#); [Minniti et al. 2021, 2024](#)), Gran 4 ([Gran et al. 2022, 2024](#)), ESO 93-08 ([Garro et al. 2023](#)), and Patchick 122 ([Garro et al. 2022, 2023](#)).

¹ <https://people.smp.uq.edu.au/HolgerBaumgardt/globular/>

We transformed the observed positions, distances and 3D velocities to the Galactocentric reference frame assuming the velocity vector of the Sun to be $(U_{\odot}, V_{\odot}, W_{\odot}) = (11.1, 12.24, 7.25) \text{ km s}^{-1}$ ([Schönrich et al. 2010](#)), the velocity of the local standard of rest $V_{LSR} = 220 \text{ km s}^{-1}$ ([Reid 2008](#)), the distance of the Sun from the Galactic centre $R_{\odot} = 8.20 \text{ kpc}$ ([GRAVITY Collaboration 2019](#)), and the height of the Sun above the Galactic plane $z_{\odot} = 20.8 \text{ pc}$ ([Bennett & Bovy 2019](#)).

The vast majority (90%) of the sample has observational errors in distances, radial velocities and proper motions along the α and δ directions of, respectively, less than 1 kpc, 2 km/s, 0.1 mas/yr, and 0.05 mas/yr. We tested that the observational errors have a negligible impact on the classification of the GCs inside the various progenitor families and show in Appendix A that this is true even for the GCs with the highest uncertainties in distance (AM 1, Eridanus, Palomar 3 and Palomar 4) and kinematical values (2MASS-GC01, AM 1 and Patchick 122).

3. Methods

The study of the GC population presented in this paper was conducted mainly using the custom-made code ORBIT. As the name implies, ORBIT is a code for orbit integrations and was designed to be customisable to suit the needs of the problem to be tackled. The decision to develop and use a custom code, rather than a well-established one, such as GALPY ([Bovy 2015](#)) or AGAMA ([Vasiliev 2019a](#)) stemmed from the desire to have complete control over the Galactic model used, each step of the orbit integration, and the available outputs. This approach allowed us to gauge the sources of errors as transparently and completely as possible and to properly evaluate realistic uncertainties in the parameters derived from the integration.

The orbital history of the GCs was computed with ORBIT backwards in time for 10 Gyr (to allow all GCs to complete more than one orbit) with a timestep of 10^4 yr . The recovered orbital parameters (see Section 3.3) were then used to identify the most likely progenitors of each GC. Starting from the classification of [Massari et al. \(2019\)](#), we reassessed the various orbital families and established memberships, focusing on relatively new GCs and previously known ones with uncertain ancestry.

3.1. General information on ORBIT

ORBIT is a code written in the C computing language and uses a “leap-frog” integration, specifically of the “kick-drift-kick” type. This choice is motivated by the fact that this is a type of modified Verlet integration ([Verlet 1967](#); [Binney & Tremaine 2008](#)) that fulfils two very important prerequisites for dynamical modelling: it is inherently time-reversible, thus allowing for both backwards and forwards integrations, and it suppresses numerical errors at each step ([Roberts & Quispel 1992](#); [Hairer et al. 2003](#)). Taken together, these characteristics ensure that the IoMs do not drift over time due to errors in the numerical approximation at each step and thus the evolution remains accurate over extremely long integrations involving a large number of steps.

The “leap-frog kick-drift-kick” scheme first computes the velocities of the tracers at the half-step $n + 1/2$, then the positions and accelerations at the full step $n + 1$, and finally updates the velocities at the full step. This scheme ensures a good approximation of the system’s evolution while performing the computationally expensive acceleration calculations only once per step. We note that while this scheme is optimal for our

use case and current model, it may not be the best solution when considering effects that explicitly depend on the velocity of tracers, such as dynamical friction for satellite galaxies (Chandrasekhar 1943a,b,c). This is because adding dynamical friction (which depends on velocity, and requires calculations to be performed twice per timestep) would slow the integration time. From a dynamical perspective, it has been demonstrated that dynamical friction has a negligible effect on the orbits of most GCs (Moreno et al. 2022) with very few exceptions for the lowest-energy ones (which would be classified as bulge GCs anyway).

As initial conditions, ORBIT requires the 6D Galactocentric phase-space coordinates of the tracers (X, Y, Z, V_x, V_y, V_z)_{gal}. The number of timesteps and tracers can be specified in a parameter file without recompiling the source code, while the step size can be modified within the source code, which requires recompilation. The source code is designed to compile without errors or warnings on the most common versions of the GNU Compiler Collection (GCC)², and it has been tested and verified on both Windows and Linux operating systems. The standard sanity check for the conservation of IoMs during integration is presented in Appendix B.

3.2. Galactic potential model

The model of the MW gravitational potential employed in ORBIT is composed of a Navarro–Frenk–White (NFW) dark matter (DM) halo (Navarro et al. 1996), two Miyamoto–Nagai (MN) stellar discs (Miyamoto & Nagai 1975), two MN gaseous discs, a Long–Murali (LM) rotating bar (Long & Murali 1992), and a spherical bulge component modelled as an Plummer profile (Plummer 1911). Finally, but with a negligible impact on the overall results, the central black hole of our Galaxy is included as a point source with mass $M_{BH} = 4.154 \times 10^6 M_\odot$ (GRAVITY Collaboration 2019).

The NFW DM halo is the most massive component of the potential, with mass $M_{DM} = 8.0 \times 10^{11} M_\odot$, scale radius $r_s = 16$ kpc and halo concentration parameter $c = 15.3$. All parameter values adopted are quite commonly used, for example in the MWPotential2014 model of Bovy (2015).

The two MN stellar discs are set up to reproduce the observed thin and thick disc of the MW. Their scale heights are fixed at $z_{thin} = 0.3$ kpc and $z_{thick} = 0.9$ kpc (i.e. McMillan 2017) and their masses and scale lengths are chosen to recover the local mass densities measured by Lian et al. (2022): $M_{thin} = 3.65 \times 10^{10} M_\odot$, $M_{thick} = 1.55 \times 10^{10} M_\odot$, $a_{thin} = 3.5$ kpc and $a_{thick} = 2.0$ kpc.

The two MN gaseous discs represent the HI and molecular gas discs observed in the MW with their masses (for a total gas mass of $M_{gas} = 1.22 \times 10^{10} M_\odot$) and scale heights fixed to the same values as the gas discs in McMillan (2017), $z_{HI} = 0.085$ kpc and $z_{HII} = 0.045$ kpc. Similar to their stellar counterparts, their scale lengths are set to reproduce the local mass densities measured for the respective gases (i.e. McKee et al. 2015), $a_{HI} = 1.824$ kpc and $a_{HII} = 5.895$ kpc.

The bulge of our model is composed of both a bar and a spherical component. The LM bar has a mass of $M_{bar} = 1.0 \times 10^{10} M_\odot$, is geometrically similar to the single-bar model in Wegg et al. (2015), with semiaxes $a_{bar} = 5.5$, $b_{bar} = 0.68$, $c_{bar} = 0.09$ kpc, an inclination angle $\alpha_{bar} = 30^\circ$, and rotating with a pattern speed $\Omega_p = 41.3 \pm 3 \text{ km s}^{-1} \text{ kpc}^{-1}$ (Sanders et al. 2019). Recent studies (i.e. Haywood et al. 2024) place the bar formation at 8–10 Gyr ago, and we verified that the results of this

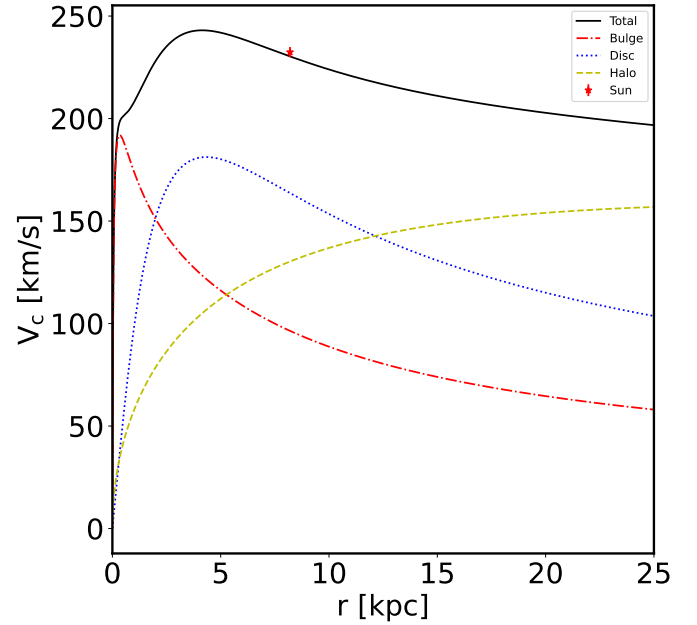


Fig. 1. Rotational curve of the MW. The solid black line shows the velocity of the full potential model, the dashed yellow line indicates the contribution from the halo component, the dotted blue line shows the total contribution from the discs and the dash-dotted red line the contribution from the bulge (bar and spheroid). The red symbol with error bar represents the Sun.

work do not change when running the integration for either 8 Gyr or 10 Gyr. The exceptions are a few high-apocentre GCs (AM 1, Crater, Palomar 3, Palomar 4 and Sagittarius II), which complete only a few orbits over the total integration time, thus their orbital parameters are slightly more accurate when using the longer integration. The evolution of the bar during its lifetime, including the change in pattern speed (Chiba et al. 2021) will be the subject of future work. The spherical component has a mass of $M_{sph} = 1.0 \times 10^{10} M_\odot$ and a scale radius of $a_{sph} = 0.3$ kpc. The geometrical parameters of both the bar and the spherical component are fitted to the Wegg et al. (2015) single-bar model which reproduced the observed density distribution of red clump giants in a “boxy/peanut” bulge shape.

The choice to include a spherical component in the bulge is motivated by observations of the MW bulge stellar populations (Valenti et al. 2016; Zoccali et al. 2018; Lim et al. 2021; Queiroz et al. 2021; Zoccali et al. 2024; Prudil et al. 2025). The total mass chosen for the MW bulge reflects the considerations presented by Shen & Zheng (2020) and the equal split between the bar and the spherical component follows Zoccali et al. (2018). Fig. 1 shows the rotation curve of the Galaxy produced by our model, including the individual contributions of the different components, which is consistent with the rotation of the Sun (red star with error bar, from Schönrich et al. 2010).

3.3. Outputs

ORBIT can be customised to produce a wide variety of outputs. In its most common configuration it provides all the classical orbital parameters, the actions, and the circularity of each tracer, and it can also output a full orbital history, recording the 6D spatial information of each tracer at every timestep.

Because the underlying potential is non-static, we expect the apocentre, R_{apo} , and pericentre, R_{peri} , (and therefore the

² <https://gcc.gnu.org/>

eccentricity, ecc) of the tracers to vary with time, making the physical significance of recovering of a single value for these parameters quite uncertain. To address this issue, the code computes R_{apo} , R_{peri} , and ecc for each complete orbit of each tracer, thereby producing a distribution of values. The mean and standard deviation of each distribution are then taken to be, respectively, the final output value and the corresponding uncertainty for each parameter. Quasi-periodic and more “well-behaved” tracers experience smaller variations in parameter values and therefore have small uncertainties, whereas tracers on chaotic orbits exhibit larger errors.

The actions (J_R, J_θ, J_ϕ) are computed following Binney & Tremaine (2008):

$$J_\phi = L_z, \quad (1)$$

$$J_\theta = L - |L_z|, \quad (2)$$

$$J_R = \frac{2}{\pi} \int_{R_{peri}}^{R_{apo}} \sqrt{2E - 2\Phi(r) - \frac{L^2}{r^2}} dr, \quad (3)$$

where L is the total angular momentum and the integral for J_R is solved numerically using a composite Simpson’s 1/3 rule (Atkinson 1991).

We further exploit the calculation of the actions to compute the following quantities:

$$J_{tot} = J_R + J_\theta + |J_\phi|, \quad (4)$$

$$J_\perp = \frac{J_\theta - J_R}{J_{tot}}, \quad (5)$$

$$J_\parallel = \frac{J_\phi}{J_{tot}}. \quad (6)$$

These ancillary parameters allow us to explore the “projected action space map” where J_\parallel is the normalised z -component of the angular momentum and J_\perp gauges the relative importance of radial and vertical motions (Vasiliev 2019b; Naidu et al. 2020; Malhan et al. 2022).

The circularity, ε , is defined as the ratio of the tracer’s angular momentum to that of a maximally rotating planar orbit, which has the same specific energy as the tracer (Abadi et al. 2003; Ruchti et al. 2014; Orkney et al. 2023):

$$\varepsilon = \frac{L_z}{L_z^{max}(E)}, \quad (7)$$

where $L_z^{max}(E)$ is found by identifying the (V_c, R_c) pair that minimises the following equation for the energy of the tracer:

$$\left| \frac{V_c^2}{2} + \Phi(R_c, 0) - E \right|, \quad (8)$$

where V_c is the circular velocity, defined as:

$$V_c = \sqrt{R_c \cdot \left. \frac{\delta\Phi}{\delta R} \right|_{R_c}}. \quad (9)$$

The full list of parameters computed with ORBIT and used throughout this work includes: R_{peri} , R_{apo} , ecc , $|Z_{max}|$ (the maximum excursion from the Galactic plane), E_{tot} , L_x , L_y , L_z , L , L_\perp (the axial, total, and perpendicular angular momenta), J_ϕ , J_θ , J_R , J_{tot} , J_\perp , J_\parallel , ε . Because of the orientation of the Galactocentric reference frame axes adopted in this work, prograde tracers have negative L_z , J_ϕ , and ε , whereas retrograde tracers have positive values of these parameters.

4. Results

Recent studies on the non-conservation of the IoMs in the MW (i.e. Pagnini et al. 2023; Woudenberg & Helmi 2025; Dillamore & Sanders 2025) caused by mergers, the secular evolution of the Galaxy, the effect of the rotating bar, and several other factors, call into question the accuracy of dynamical analyses. This is the principal reason why, instead of focusing solely on the IoMs and/or adiabatic invariants, this work presents a full sample of dynamical spaces (six spaces for ten different parameters), which helps in characterising the various progenitors. For each progenitor, differences in the way the accretion event happened, its age, the mass of the accreted structure, and many other factors, result in distinct signatures across different parameter spaces. The ability to explore a vast, multidimensional parameter space is fundamental for highlighting features and trends that allow discrimination between the numerous orbital families present in our Galaxy.

The main results of our orbital analysis are summarised in Table 1, which lists the GCs studied and their most likely progenitor. Figure 2 provides an overview of the composition of the orbital families in the commonly used L_z – E_{tot} space. Throughout this section, we highlight the main signatures in the various parameter spaces of the most important substructures in the MW and provide boundaries for the values of the dynamical parameters deemed most important for assigning a GC to a given progenitor. To determine whether a GC belongs to a particular family, we examined which “locus” it tracks across the most dynamical parameter spaces (ideally all). Here and elsewhere in the paper we define the locus of a substructure as the region of dynamical space populated by bona fide tracers belonging to it. Some parameter spaces do not explicitly allow to discriminate between prograde and retrograde tracers, but this distinction is often useful for resolving apparent overlaps between families (i.e. in Fig. 3, the green circles of retrograde GCs and the yellow circles of Helmi Streams GCs overlap, but the two families are clearly separated by their sign of L_z). In Sect. 5 we discuss the edge cases of GCs with the most uncertain associations.

4.1. Structures considered and absent progenitors

This work focuses on the following structures: the disc and bulge of the MW (making up the in-situ component), Gaia-Enceladus-Sausage (GES, Koppelman et al. 2018; Belokurov et al. 2018; Haywood et al. 2018; Helmi et al. 2018), Sagittarius (Sag, Ibata et al. 1994; Majewski et al. 2003), the Helmi Streams (HS, Helmi et al. 1999; Koppelman et al. 2019b), the retrograde halo (with a detailed discussion in Sect. 5.2), the low energy group (low-E, first labelled by Massari et al. 2019, with a detailed discussion in Sect. 5.1), Aleph (Naidu et al. 2020), Cetus (Newberg et al. 2009; Yuan et al. 2019, 2022), Typhon (Tenachi et al. 2022), and Elqui (Shipp et al. 2018, 2019).

In our analysis, we seemingly omitted some known substructures, either because the progenitor locus substantially overlaps with well-known structures or because limited data prevented us from properly identifying the progenitor. In both instances, this made it impossible to dynamically distinguish the newer candidates from well-established structures. For LMS-1/Wukong (Naidu et al. 2020; Yuan et al. 2020), the stellar component identified by Malhan et al. (2024) overlaps with the loci of the HS and GES progenitors across all parameter spaces. The loci identified for Shakti and Shiva (Malhan & Rix 2024) substantially overlap with those of the disc and low-E groups, whereas it has not been possible to produce suitable datasets to identify the loci of Icarus

Table 1. Identification of GC progenitors based on the dynamical analysis carried out in this work.

Cluster	Progenitor	Cluster	Progenitor	Cluster	Progenitor	Cluster	Progenitor
2MASS-GC01	Disc	NGC 4590	HS	NGC 6362	Disc	NGC 6864	GES
2MASS-GC02	Disc	NGC 4833	GES	NGC 6366	Disc	NGC 6934	Unk
AM 1	Elqui	NGC 5024	HS	NGC 6380	Bulge	NGC 6981	GES
AM 4	Unk	NGC 5053	HS	NGC 6388	low-E	NGC 7006	Retro
Arp 2	Sag	NGC 5139	Retro/Thamnos	NGC 6397	Disc	NGC 7078	Disc
BH 140	Unk	NGC 5272	HS	NGC 6401	Bulge	NGC 7089	GES
BH 261	Disc	NGC 5286	GES	NGC 6402	low-E	NGC 7099	GES
Crater	Unk	NGC 5466	Retro	NGC 6426	HS	NGC 7492	GES
Djor 1	Unk	NGC 5634	HS	NGC 6440	Bulge	Pal 1	Aleph
Djor 2	Bulge	NGC 5694	Retro	NGC 6441	Disc	Pal 2	GES
E 3	Aleph	NGC 5824	HS	NGC 6453	Bulge	Pal 3	Cetus
Eridanus	Sag	NGC 5897	Unk	NGC 6496	Disc	Pal 4	Cetus
ESO 93-08	Aleph/Disc	NGC 5904	GES	NGC 6517	Bulge	Pal 5	HS
ESO 280-SC06	GES	NGC 5927	Disc	NGC 6522	Bulge	Pal 6	Bulge
ESO 452-C11	Bulge	NGC 5946	low-E	NGC 6528	Bulge	Pal 8	Disc
FSR 1713	Disc	NGC 5986	low-E	NGC 6535	low-E	Pal 10	Aleph/Disc
FSR 1735	Disc	NGC 6093	low-E	NGC 6539	Disc	Pal 11	Disc
FSR 1758	Retro/Thamnos	NGC 6101	Retro/Antaeus	NGC 6540	Bulge	Pal 12	Sag
Gran 1	Bulge	NGC 6121	GES	NGC 6541	Disc	Pal 13	Retro
Gran 2	Retro/Thamnos	NGC 6139	Disc	NGC 6544	low-E	Pal 14	Typhon
Gran 3	Unk	NGC 6155	low-E	NGC 6553	Disc	Pal 15	Typhon
Gran 4	HS	NGC 6171	Disc	NGC 6558	Bulge	Patchick 122	Disc
Gran 5	Bulge	NGC 6205	GES	NGC 6569	Disc	Patchick 126	Disc
HP 1	Bulge	NGC 6218	Disc	NGC 6584	GES/HS	Pyxis	Elqui
IC 1257	GES	NGC 6229	GES	NGC 6624	Bulge	Rup 106	HS
IC 1276	Disc	NGC 6235	Disc	NGC 6626	Bulge	Sag II	Unk
IC 4499	Retro	NGC 6254	Disc	NGC 6637	Bulge	Ter 1	Bulge
Laevens 3	Sag	NGC 6256	Bulge	NGC 6638	Bulge	Ter 2	Bulge
Liller 1	Bulge	NGC 6266	Bulge	NGC 6642	Bulge	Ter 3	Disc
Lynga 7	Disc	NGC 6273	low-E	NGC 6652	Bulge	Ter 4	Bulge
NGC 104	Disc	NGC 6284	Unk	NGC 6656	Disc	Ter 6	Bulge
NGC 288	Retro	NGC 6287	low-E	NGC 6681	low-E	Ter 7	Sag
NGC 362	GES	NGC 6293	Bulge	NGC 6712	low-E	Ter 8	Sag
NGC 1261	GES	NGC 6304	Disc	NGC 6715	Sag	Ter 9	Bulge
NGC 1851	GES	NGC 6316	Disc	NGC 6717	Bulge	Ter 10	low-E
NGC 1904	GES	NGC 6325	Bulge	NGC 6723	Unk	Ter 12	Disc
NGC 2298	GES	NGC 6333	low-E	NGC 6749	Disc	Ton 2	Disc
NGC 2419	Sag	NGC 6341	GES	NGC 6752	Disc	UKS-1	GES
NGC 2808	GES	NGC 6342	Bulge	NGC 6760	Disc	VVV-CL001	Bulge
NGC 3201	Retro/Antaeus	NGC 6352	Disc	NGC 6779	GES	VVV-CL002	Bulge
NGC 4147	GES	NGC 6355	Bulge	NGC 6809	low-E	VVV-CL160	GES
NGC 4372	Disc	NGC 6356	Disc	NGC 6838	Disc	Whiting 1	Sag

Notes. The progenitors are the following: Aleph, Antaeus, bulge, Cetus, disc, Elqui, Gaia-Enceladus-Sausage (GES), Helmi Streams (HS), low energy group (low-E), Sagittarius (Sag), retrograde family (retro), Thamnos, Typhon, and unknown (Unk).

(Re Fiorentin et al. 2021, 2024) and Pontus (Malhan et al. 2022; Malhan 2022). In the case of Nyx (Necib et al. 2020b,a, 2022), we do not include it in our analysis due to mounting evidence that it does not represent an independent merger event (Horta et al. 2023; Wang et al. 2023).

4.2. Bulge

The MW bulge GC population is characterised by the presence of the least energetic GCs (cyan circles in Fig. 2). While all types of orbits (prograde, retrograde or radial) are possible, the value of $|L_z|$ remains close to zero for all members of this group as they reside in the deepest part of the MW potential well. Similarly,

with orbits largely confined to the bulge, these GCs occupy the bottom-left corner of $R_{apo} - R_{peri}$ space (Fig. 3). We define bulge GCs as those with:

- $E_{tot} < -1.75 \times 10^5 \text{ km}^2/\text{s}^2$
- $R_{peri} < 1.5 \text{ kpc}$
- $R_{apo} < 3.5 \text{ kpc}$.

4.3. Disc

Although there are subtle kinematical differences between the populations of tracers inhabiting the thin and thick discs of the MW, their dynamical distributions largely overlap and the two structures are better separated through chemical analysis (i.e.

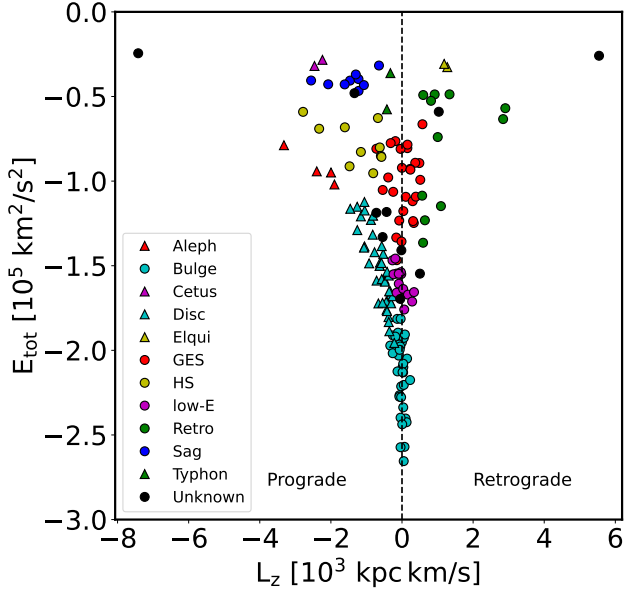


Fig. 2. Globular cluster sample in the angular momentum versus total energy plane. The symbols denote the affiliation to specific progenitor, as indicated in the legend: red triangles for Aleph, cyan circles for the bulge, purple triangles for Cetus, cyan triangles for the disc, yellow triangles for Elqui, red circles for Gaia-Enceladus-Sausage (GES), yellow circles for the Helmi Streams (HS), purple circles for the low energy group (low-E), green circles for the retrogrades (retro), blue circles for Sagittarius (Sag), green triangles for Typhon, and black circles for the unassociated clusters. The dashed line at $L_z = 0$ marks the division between prograde and retrograde sides.

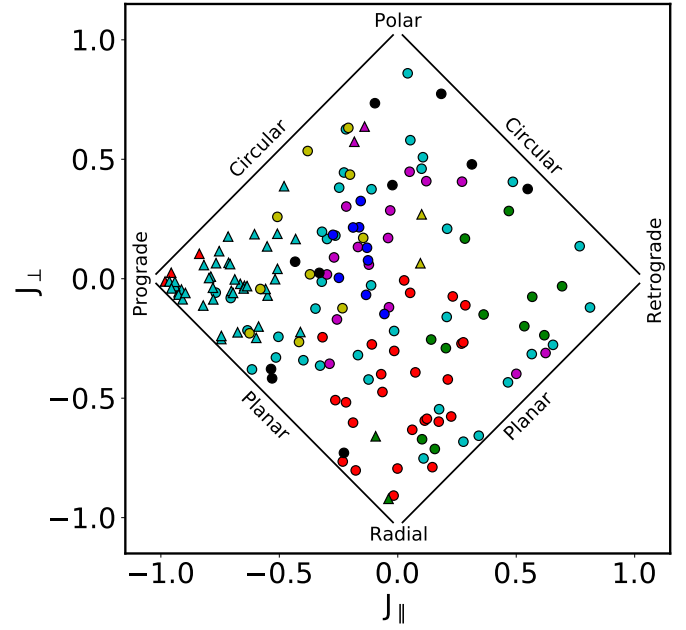


Fig. 4. Globular cluster sample in the parallel versus perpendicular action space. GCs with $J_{\parallel} \approx -1$ are on nearly circular prograde orbits, whereas those with $J_{\parallel} \approx 1$ are on nearly circular retrograde orbits. GCs with $J_{\perp} \approx -1$ follow radial orbits while those with $J_{\perp} \approx 1$ are on polar orbits. The GCs are marked according to their identified progenitor as in Fig. 2.

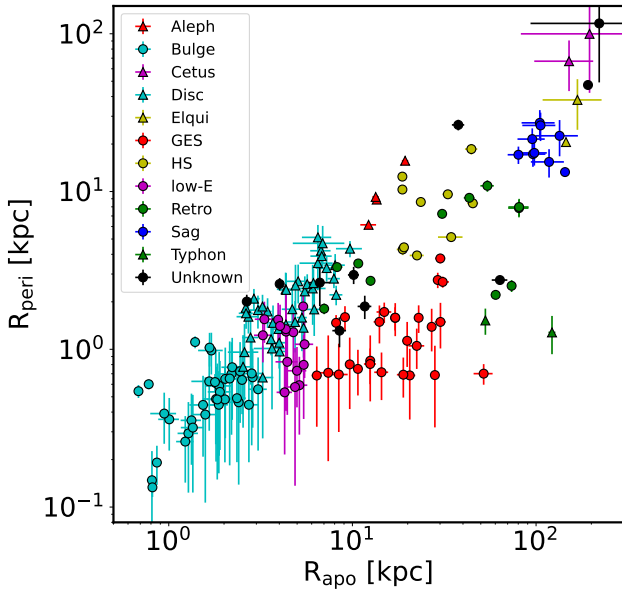


Fig. 3. Globular cluster sample in the apocentre versus pericentre plane, shown on a logarithmic scale. The uncertainties are computed as detailed in Sect. 3.3. The GCs are marked according to their identified progenitor, as in Fig. 2.

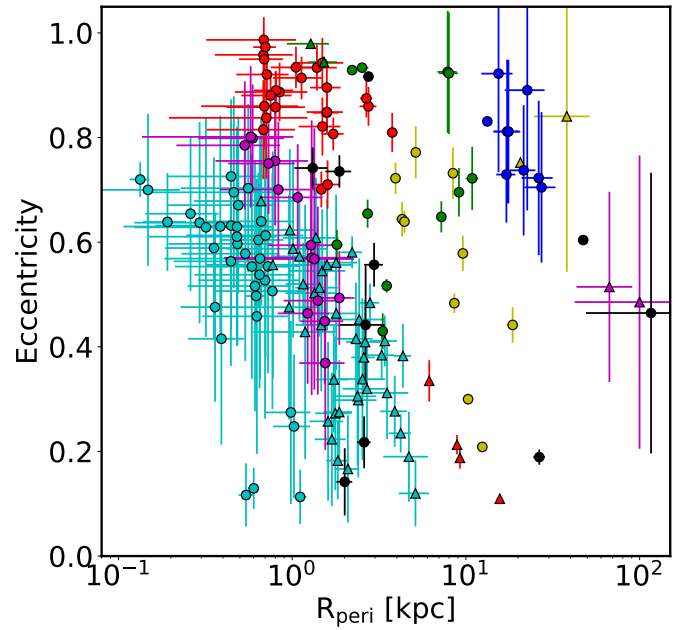


Fig. 5. Globular cluster sample in the pericentre versus eccentricity plane, shown on a semi-logarithmic scale. The uncertainties are computed as detailed in Sect. 3.3. The GCs are marked according to their identified progenitor as in Fig. 2.

Bensby et al. 2014; Hayden et al. 2015). For this reason, we treat both thin- and thick-disc populations as a single structure. The MW disc is quite prominently visible in the prograde portion of the L_z - E_{tot} space (cyan triangles in Fig. 2). Consequently, the main features of disc GCs are $\varepsilon \approx J_{\parallel} \leq -0.5$ (usually

similar values, as both gauge the rotational support of an orbit) and $ecc \leq 0.6$. Disc GCs are also clearly identified in the most prograde sector of the $J_{\parallel} - J_{\perp}$ space (Fig. 4) and trace a characteristic sequence in the $R_{peri} - ecc$ space (Fig. 5). Disc GCs generally exhibit the following defining characteristics:

- $-2.0 \times 10^5 \text{ km}^2/\text{s}^2 < E_{tot} < -1.1 \times 10^5 \text{ km}^2/\text{s}^2$
- $L_z < 0 \text{ kpc km/s}$
- $0.6 \text{ kpc} < R_{peri} < 6 \text{ kpc}$
- $Ecc < 0.7$
- $J_{||}/\varepsilon < -0.4$.

4.4. Gaia–Enceladus–Sausage (GES)

As the most massive accretion event of our Galaxy, the GES is prominently visible as a central, mildly energetic overdensity in the L_z – E_{tot} space (red circles in Fig. 2). The population of GCs associated with this event is characterised by radial orbits (Fig. 4) with high ecc at relatively low R_{peri} (Fig. 5). The GES GCs are characterised by:

- $-1.5 \times 10^5 \text{ km}^2/\text{s}^2 < E_{tot} < -0.6 \times 10^5 \text{ km}^2/\text{s}^2$
- $Ecc > 0.7$
- $4 \text{ kpc} < Z_{max} < 40 \text{ kpc}$
- $-0.3 < J_{||}/\varepsilon < 0.3$
- $J_{\perp} < 0.0$.

4.5. Sagittarius (Sag)

The ongoing merger of the Sagittarius dwarf galaxy is the most recent accretion event to affect our Galaxy, and remains visible in the sky as a wide, long stellar stream. The GCs associated with the Sag event exhibit highly energetic, prograde orbits (blue circles in Fig. 2), are among those with the highest R_{peri} and R_{apo} (Fig. 3) and also have high L_{\perp} (Fig. 6). We define Sag GCs as those satisfying:

- $E_{tot} > -0.5 \times 10^5 \text{ km}^2/\text{s}^2$
- $-3.0 \times 10^3 \text{ kpc km/s} < L_z < -0.5 \times 10^3 \text{ kpc km/s}$
- $4.0 \times 10^3 \text{ kpc km/s} < L_{\perp} < 7 \times 10^3 \text{ kpc km/s}$.

4.6. Helmi Streams (HS)

The progenitor of the Helmi Streams was among the first accreted substructures identified through the study of IoMs. The population belonging to this accretion event is characterised by prograde, high-energy orbits between the disc and the Sag populations in the L_z – E_{tot} space (yellow circles in Fig. 2). The HS GCs also occupy a well-defined portion of the L_z – L_{\perp} plane (Fig. 6) and a distinctive sequence in R_{peri} – ecc space (Fig. 5). Our selection criteria for HS GCs are:

- $-1.0 \times 10^5 \text{ km}^2/\text{s}^2 < E_{tot} < -0.5 \times 10^5 \text{ km}^2/\text{s}^2$
- $L_z < -0.5 \times 10^3 \text{ kpc km/s}$
- $1.0 \times 10^3 \text{ kpc km/s} < L_{\perp} < 4.0 \times 10^3 \text{ kpc km/s}$.

4.7. Retrogrades

The full characterisation of the retrograde portion of the halo is an ongoing effort that has seen several candidate merger events proposed over recent years. Since some of the candidate progenitors have been discarded, the consensus on others is still to be reached, and new ones continue to be proposed, we refer to Sect. 5.2 for a more in-depth discussion of each progenitor and here limit ourselves to sketching the defining traits of the retrograde family as a whole. The retrograde GCs can be clearly distinguished in L_z – L_{\perp} space (Fig. 6) and populate a distinctive diagonal streak of increasing ε with decreasing $|Z_{max}|$ (Fig. 7). We identify as members of this group the GCs that satisfy:

- $E_{tot} > -1.5 \times 10^5 \text{ km}^2/\text{s}^2$
- $L_z > 0.5 \times 10^3 \text{ kpc km/s}$
- $Z_{max} > 4 \text{ kpc}$.

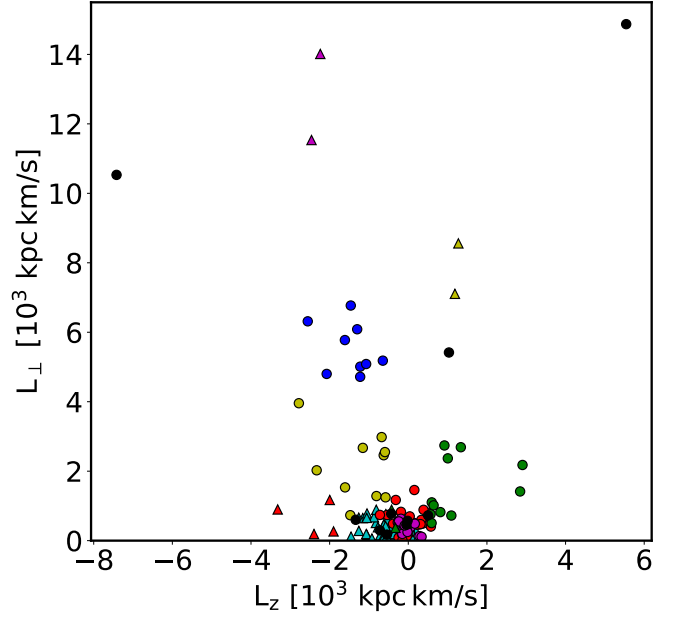


Fig. 6. Globular cluster sample in the vertical versus perpendicular angular momentum plane. As shown in this figure, most GCs are crowded in the low L_{\perp} region, where the loci of different progenitors overlap. However this space is very useful for distinguishing the various high-energy families. The GCs are marked according to their identified progenitor as in Fig. 2.

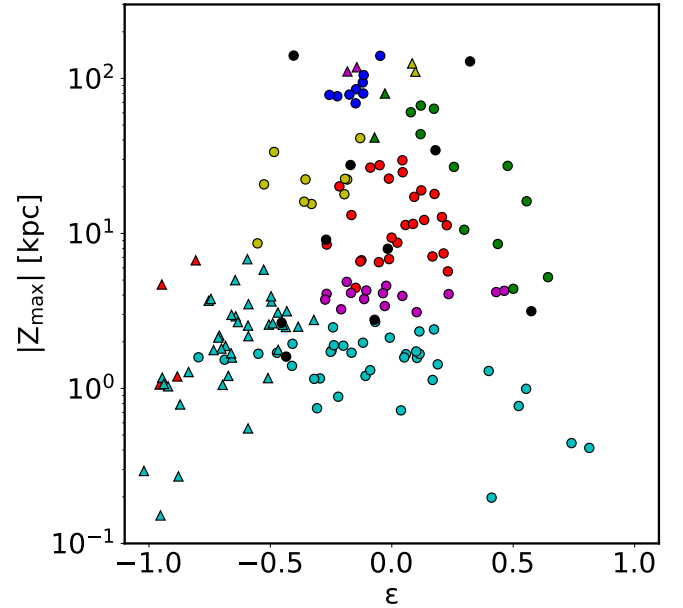


Fig. 7. Globular cluster sample in the circularity versus maximum vertical excursion plane, shown on a semi-logarithmic scale. The GCs are marked according to their identified progenitor as in Fig. 2.

4.8. Low-energy group (low-E)

This group has been associated with various accretion events and in-situ structures and for the moment we retain this general label. The GCs associated with this group are characterised by energies lower than those of GES but higher than those of the bulge, and by small values of $|L_z|$ (purple circles in Fig. 2). Similarly, GCs in the low-E group populate a region of mid ε and Z_{max} (Fig. 7). Low-E GCs generally exhibit the following:

- $-1.8 \times 10^5 \text{ km}^2/\text{s}^2 < E_{tot} - 1.4 \times 10^5 \text{ km}^2/\text{s}^2$
- $0.5 \text{ kpc} < R_{peri} < 2 \text{ kpc}$
- $3 \text{ kpc} < R_{apo} < 6 \text{ kpc}$
- $3 \text{ kpc} < Z_{max} < 6 \text{ kpc}$
- $-0.5 < \varepsilon < 0.5$.

4.9. Other structures

As already noted, the wealth of data that has become available over roughly the last decade has enabled the population of wider regions of the dynamical parameter spaces and has highlighted smaller confirmed and candidate merger events. The following progenitors each have only a small number of associated GCs.

4.9.1. Aleph

This structure appears to be a direct continuation of the disc at high energies and includes some of the most prograde GCs (red triangles in Fig. 2). The GCs belonging to this progenitor also exhibit higher R_{peri} and R_{apo} than their counterparts in the disc (Fig. 3). The Aleph GCs have:

- $E_{tot} > -1.1 \times 10^5 \text{ km}^2/\text{s}^2$
- $R_{peri} > 5 \text{ kpc}$
- $R_{apo} > 10 \text{ kpc}$
- $Ecc < 0.4$
- $L_z < -1.75 \times 10^3 \text{ kpc km/s}$.

4.9.2. Cetus

This merger, identified as a stream on a very polar orbit, is composed of prograde and very energetic tracers and lies very close to Sag in L_z - E_{tot} space (purple triangles in Fig. 2). It is possible to distinguish genuine members of the Cetus merger for their extremely high R_{peri} , R_{apo} (Fig. 3), L_\perp (Fig. 6), and almost fully polar orbits (Fig. 4). The GCs belonging to Cetus exhibit the following:

- $E_{tot} > -0.5 \times 10^5 \text{ km}^2/\text{s}^2$
- $L_z \approx -2.0 \times 10^3 \text{ kpc km/s}$
- $L_\perp > 11.0 \times 10^3 \text{ kpc km/s}$.

4.9.3. Typhon

This is another merger discovered as a surviving stream with a long, radial orbit. We tentatively associate two high-energy GCs with this progenitor. These GCs partially overlap in some parameter spaces with the Typhon stellar populations identified by Tenachi et al. (2022) and Dodd et al. (2023) and are characterised by radial orbits (green triangles in Fig. 4) and very high R_{apo} coupled with very low R_{peri} (Fig. 3). We tentatively identify Typhon GCs as those having:

- $E_{tot} > -0.7 \times 10^5 \text{ km}^2/\text{s}^2$
- $1.0 \text{ kpc} < R_{peri} < 2.0 \text{ kpc}$
- $R_{apo} > 50 \text{ kpc}$
- $Z_{max} > 40 \text{ kpc}$.

4.9.4. Elqui

The debris stream produced by this merger is one of the most distant identified (Shipp et al. 2018, 2019). The associated GCs are retrograde and at high energies (yellow triangles in Fig. 2) but they have much higher R_{peri} , R_{apo} (Fig. 3), and L_\perp (Fig. 6) than those of the retrograde group. Being quite isolated from the rest of the retrograde family in almost all dynamical spaces, we

are confident in assigning two GCs directly to Elqui. These GCs exhibit the following:

- $E_{tot} > -0.5 \times 10^5 \text{ km}^2/\text{s}^2$
- $L_z \approx 1.0 \times 10^3 \text{ kpc km/s}$
- $7.0 \times 10^3 \text{ kpc km/s} < L_\perp < 9.0 \times 10^3 \text{ kpc km/s}$.

5. Discussion

The main difference between this work and most studies in the literature is the inclusion of the rotating bar of the MW in the model underlying the orbital integration. We tested the direct effect of including or excluding the bar by running ORBIT with and without the rotating bar and comparing the resulting outputs. The main effect of the bar is to alter the pericentres and eccentricities of GCs roughly below $E_{tot} = -1.7 \times 10^5 \text{ km}^2/\text{s}^2$ and of some clusters with highly radial orbits (i.e. very small pericentres). This translates into some changes in the classification of the GCs in the lowest-energy groups (bulge, disc, GES, and low-E), while the classification of GCs belonging to the other families is largely unaffected. Without the bar, Gran 5, NGC 6517, and NGC 6626 (all previously classified as bulge GCs), NGC 6121 (previously GES), NGC 6723 (previously unclassified), and NGC 6171 (previously disc) would instead be classified as low-E GCs. Three clusters (NGC 6256, NGC 6266, and NGC 6540) would move from the bulge to the disc family, while one (2MASS-GC02) would move from the disc to the bulge family. Finally, NGC 6284 would be classified as a GES member. These changes in the associations between GCs and progenitors make our overall classification much closer to that reported in the literature (i.e. Massari et al. 2019) because our model without a bar is essentially a variant of the widely used McMillan (2017) model.

5.1. Outliers within the groups

Although we identified defining characteristics for each family, some members stand due to their peculiar properties. In the following, we discuss these cases and the GCs contended between groups.

Starting from the bulge, it is important to mention the small number of GCs with ε and J_\parallel values indicative of highly counter-rotating orbits (the cyan circles at the bottom right of Fig. 7 with $\varepsilon > 0.4$). These GCs, VVV-CL001, Djor 2, Terzan 2, Terzan 6, Liller 1, and NGC 6325, appear clearly separated from the main bulge population due to their peculiar kinematics. Tests indicate that the spherical component of the bulge is partly responsible for their extreme kinematics. However, even when this component is removed, these GCs remain on clearly counter-rotating orbits (though less extreme). Gran 1 stands out for another reason: it is one of the least eccentric GCs in the sample, with a highly polar orbit confined to the inner bulge (topmost cyan circle at $J_\perp \approx 1.0$ in Fig. 4).

At the interface between the bulge and disc groupings, there are four GCs with fairly circular orbits (cyan circles with $J_\parallel \geq 0.6$ in Fig. 4). Despite this, NGC 6256, NGC 6266, NGC 6540, and Terzan 1 reside deep within the potential well, with very small R_{apo} and R_{peri} , and therefore we assign them to the bulge. In contrast, 2MASS-GC02 is the least energetic of the disc GCs, but its R_{apo} and R_{peri} are not small enough for it to reside in the bulge region, so we assign it to the disc family. Four of these five GCs are exactly those that move between the bulge and disc families depending on the presence or absence of the rotating bar (Sect. 5), demonstrating the influence of different choices of bulge models.

Moving on to the low-E group, it has historically been the home of tracers that could not be unambiguously attributed to either GES or the MW bulge. Several authors have linked some or all members of this group to different accretion events, namely Kraken (Krujissen et al. 2019, 2020), Koala (Forbes 2020), and Heracles (Horta et al. 2021), which may represent the same structure. Other works have highlighted in-situ populations with similar chemo-kinematical signatures, namely Aurora (Belokurov & Kravtsov 2022; Myeong et al. 2022), Poor Old Heart (Rix et al. 2022), arguing that these structures (both accreted and in-situ) are the different facets of the same stellar population constituting the proto-Galaxy. Nevertheless, due to their tight distribution across dynamical parameter spaces, we have kept these clusters grouped together. The only two significant outliers within this family are NGC 6388 and NGC 6535, which are the most retrograde and planar low-E GCs (the rightmost purple circles in Fig. 7). Both GCs, while very retrograde, do not have sufficient energy to connect with the retrograde family or with the hypothesised Thamnos members (discussed in Sect. 5.2). Interestingly, they remain quite close in all parameter spaces, which may hint at a shared history.

The GES group of GCs contains several minor outliers. Pal 2 is among the most energetic GES GCs, exhibiting a highly radial orbit, very low R_{peri} , and very high R_{apo} (rightmost red circle in Fig. 3) and $|Z_{max}|$. However, all the other parameters identify it as a belonging to the GES progenitor. NGC 5904 and NGC 7492 are compatible with GES in most parameter spaces but have the highest L_{\perp} and R_{peri} of the family. Similarly, the high ecc and radial orbit of NGC 6584 identify it as a GES GC despite its very high $|Z_{max}|$ and R_{peri} (these three GCs are the highest red circles in Fig. 3). NGC 6205 and NGC 7099 fit quite well within the GES family except for their uncharacteristically low ecc (red circles at $ecc \approx 0.7$ in Fig. 5). Given the nature of GES as the most massive merger event of the MW, it is quite possible for its dynamical signature to be less compact than those of smaller and more recent mergers (i.e. Sag), with a modest number of outliers (six out of 26 GCs).

In the prograde and higher energy space, ESO 93-08 and Pal 10 are the two GCS with uncertain attribution to the Aleph structure (lowest red triangles in Fig. 7). Although they have a higher E_{tot} and $|L_z|$ than disc GCs, they have much lower $|Z_{max}|$ and L_{\perp} than the other members of Aleph and may instead be the outermost disc GCs. Given the uncertainty in the nature and characteristics of the Aleph progenitor, it remains unclear whether these GCs are more closely linked to the disc.

NGC 4590, NGC 5824, and NGC 6426 are the GCs on the most prograde circular orbits within the HS family (yellow circles with $J_{\parallel} < -0.5$ in Fig. 4), similar to disc GCs, but with R_{apo} , Z_{max} , and L_{\perp} values consistent with the HS group and lying on the HS sequence in $R_{peri} - ecc$ space. The presence of debris on prograde orbits is expected from a merger generally believed to be prograde (even if not planar) and relatively massive at the time of accretion (Helmi et al. 1999).

The Sag group is well isolated across all parameter spaces with only Eridanus being slightly an outlier due to its higher $|Z_{max}|$.

5.2. The retrograde family

The retrograde halo has been populated by several candidate progenitors over the years, starting with Sequoia (Myeong et al. 2018; Barbá et al. 2019; Matsuno et al. 2019; Myeong et al. 2019) and Elqui (Shipp et al. 2018, 2019) to several more. Studies based

on simulations of the complex dynamics of galactic mergers suggest that high mass-ratio events spread their debris across large portions of parameter space, spilling copiously in the retrograde portion of the halo, and causing these debris to be mistaken for independent mergers (Koppelman et al. 2020; Amarante et al. 2022; Khoperskov et al. 2023). Arjuna (proposed by Naidu et al. 2020) has been rejected for this very reason and its sibling I'toi (from the same work) is under similar scrutiny, hampered by a dearth of chemical information (Naidu et al. 2021; Horta et al. 2023).

Thamnos (Koppelman et al. 2019a) is another candidate member of the retrograde family, first identified as a pair of overdensities very close to each other in the mid-energy, retrograde portion of the $L_z - E_{tot}$ space. Koppelman et al. (2019a) and subsequent works estimated a very low mass for the Thamnos progenitor ($M_{Thamnos} \leq 5 \cdot 10^7 M_{\odot}$), making it very unlikely that it would harbour any GC capable of surviving the merger while retaining a recognisable dynamical signature to the present time. Moreover, recent work on the chemical characterisation of substructures seems to indicate that the stellar population of Thamnos is heavily contaminated by in-situ and GES tracers (i.e. Fig. 15 from Ruiz-Lara et al. 2022). Nevertheless, based on a purely dynamical analysis, several clusters unassociated with other progenitors or within the retrograde family fall in or near the loci identified by the Thamnos stellar component in the various dynamical spaces. NGC 5139 (also known as ω Cen) and FSR 1758 are the GCs that most closely track the Thamnos stellar population across all parameter spaces while Gran 2 exhibits a slightly out-of-plane, more polar orbit (with higher $|Z_{max}|$ and L_{\perp}). The aforementioned NGC 6388 and NGC 6535 exhibit retrograde planar orbits very similar to those of the Thamnos tracers, however they reside much deeper in the MW potential well and have lower E_{tot} , R_{apo} , and R_{peri} .

Antaeus/L-RL64 is an extremely retrograde and highly energetic merger remnant identified by Oria et al. (2022) and Ruiz-Lara et al. (2022). More recently, the small structure of ED-3 has been identified in the retrograde halo (Dodd et al. 2023), occupying loci that are connected or contiguous to Antaeus/L-RL64 in all parameter spaces. The association between the two structures has been corroborated by the findings of Ceccarelli et al. (2024). Based on their strongly retrograde orbits, NGC 3201 and NGC 6101 could be associated with this structure. Although the two clusters do not directly track the stars identified as Antaeus members by Oria et al. (2022) and Dodd et al. (2022), NGC 3201 closely follows the loci of ED-3 members across all dynamical spaces, allowing us to establish a tentative association between these two GCs and the Antaeus progenitor.

5.3. Unclassified GCs

Some MW GCs share some defining characteristics with the aforementioned groups but appear strongly discordant in other parameter spaces. We briefly review these outliers that cannot be unequivocally assigned to any progenitor.

AM-4 lies amid the retrograde group in $L_z - E_{tot}$ space but has a much higher R_{peri} and much lower ecc that distinguish it as a clear extreme outsider within this family. Crater is too extreme in all parameter spaces to be a part of any retrograde family. Sagittarius II is Crater's counterpart in the prograde portion of dynamical space, being a distant outlier from all identified groups. NGC 6934 is too energetic for, and has a higher R_{apo} than, Helmi Streams GCs but has R_{peri} and $|Z_{max}|$ too low for Sag GCs, and its orbit is too radial for both families. Located between the loci of the low-E and GES families, NGC 6284

has R_{apo} , R_{peri} , and $|Z_{max}|$ value that are too high to belong to the former group and ecc that is too low, together with a more polar than radial orbit, to be classified as a GES GC. BH 140 and Djor 1 have many characteristics of disc GCs, with prograde and circular orbits, but their R_{apo} , R_{peri} , and ecc values are too high compared to the other disc GCs. The orbit of NGC 5897 is not circular enough for it to be a (thick) disc GC and not radial enough to belong to the GES. Similarly, its R_{apo} , R_{peri} , and $|Z_{max}|$ values are too high for the disc population and its ecc is too low for the GES. Gran 3 has a retrograde circular orbit with a very low ecc , which distinguishes it from nearby identified groups at similar energies. NGC 6723 likewise has a very low ecc (making its membership in the low-E group very unlikely) and is characterised by a peculiar, extremely polar orbit.

5.4. Literature comparison

Reviewing some recent literature on the classification of the MW GC population, we do not compare directly our work with that of [Bica et al. \(2024\)](#), as their selection is based on ages and chemistry, whereas ours relied solely on dynamical information. Similarly, the selection presented by [Belokurov & Kravtsov \(2024\)](#), while incorporating some dynamical information, is guided and calibrated using the $[Al/Fe]$ abundance ratio and only distinguishes between the in-situ and accreted components. Nevertheless, we find general agreement with the classification by [Belokurov & Kravtsov \(2024\)](#), with the notable exception of the low-E family, whose members the authors mostly classify as in-situ (likely attributing them to the Aurora population, [Belokurov & Kravtsov 2022](#)). For the families identified in both studies, we also find general agreement with [Chen & Gnedin \(2024\)](#), again with the notable exception of the low-E group, identified as in-situ by these authors. Our results agree closely with the classification of high- and mid-energy GCs by [Callingham et al. \(2022\)](#); [Sun et al. \(2023\)](#); [Massari \(2025\)](#), but differs for the lowest-energy groups (bulge, disc, and low-E). All these studies use as an underlying model the static potential from [McMillan \(2017\)](#), and it is clear that discrepancies in the classification of the least energetic GCs arise from the impact of the rotating bar on the orbital parameters. In the case of [Massari \(2025\)](#) it is worth also noting that part of the differences are due to these authors not including Aleph in their list of progenitors, whereas we slightly unpacked their “high energy” group into some known progenitors (and Typhon). We note several differences with respect to the classification by [Malhan et al. \(2022\)](#) primarily due to their adoption of a partially different set of progenitors, namely LMS-1/Wukong, Pontus, and an unknown retrograde merger (see Sect. 4.1 for our reasons for excluding these progenitors). One of the first studies to employ an underlying potential including a rotating bar is [Pérez-Villegas et al. \(2020\)](#), however they use a different classification (bulge, disc, inner halo, and outer halo) and without distinguishing between the various merger events. Nevertheless our lists of bulge and disc clusters closely agree, with minor discrepancies due to the different ecc threshold used to define disc membership. Another study incorporating a rotating bar into the underlying potential is [Garro et al. \(2023\)](#), which focuses on a small subsample of clusters. Our results are in broad agreement with theirs, with orbital parameters consistent within the errors.

6. Conclusions

We present ORBIT, a new in-house tool for precise and efficient orbit integration to study galactic dynamics. The code’s novelty

resides in fully accounting for a time-varying potential at all stages, especially for the recovery of the orbital parameters and their associated uncertainties. ORBIT, with its up-to-date potential model of the MW including the rotating bar and a spherical bulge component, has already been used to characterise the RR Lyrae population of the bulge ([Olivares Carvajal et al. 2024](#)). In this work, we used ORBIT to study the dynamics of the galactic GCs and to classify them among the various families of merger events.

Using information derived from six different dynamical parameter spaces (orbital parameters, IoMs, and adiabatic invariants), we provide a full dynamical characterisation of the in-situ population and different progenitors. Including the rotating bar changes the associations of low-energy GCs, while our comprehensive dynamical analysis enables clear associations for a number of previously unassociated high-energy GCs to specific structures (four GCs to Aleph and two each to Cetus, Typhon, Elqui and Antaeus). We also propose the association of three GCs to the Thamnos progenitor, further complicating the conundrum posed by this very small, old merger.

Several GCs remain of ambiguous ancestry or are clear outliers within their families, and some still lack any associated progenitor. This work represents a step towards complete characterisation of the MW inventory, and our purely dynamical view must be complemented with cutting-edge chronochemical studies (i.e. the CARMA project, [Massari et al. 2023](#); [Aguado-Agelet et al. 2025](#); [Ceccarelli et al. 2025](#)).

In future work, we will explore the effect of the rotating bar in more depth, including both its direct gravitational pull affecting the central region of the MW and the resonances it generates as a time-varying component of the potential.

Data availability

The data underlying this article come from public sources listed in Section 2. The full table C.1 is available at the CDS via <https://cdsarc.cds.unistra.fr/viz-bin/cat/J/A+A/706/A130> (an excerpt of the table is provided in Appendix C).

Acknowledgements. The authors would like to thank the anonymous referee for insightful comments that helped improve and clarify the manuscript. Thanks also go to D. Massari, E. Ceccarelli, M. Bellazzini, A. Mucciarelli and E. Dodd for valuable discussions. MDL acknowledges financial support from the National Agency for Research and Development (ANID), Millennium Science Initiative, ICN12_009 and from the project “LEGO – Reconstructing the building blocks of the Galaxy by chemical tagging” (PI: Mucciarelli) granted by the Italian MUR through contract PRIN2022LLP8TK_001. MZ acknowledges support by the National Agency for Research and Development (ANID) Millennium Science Initiative, ICN12_009 and AIM23-0001, awarded to the Millennium Institute of Astrophysics (MAS) and the ANID BASAL Center for Astrophysics and Associated Technologies (CATA) through grant FB210003, and from ANID FONDECYT Regular No. 1230731. BA-T acknowledges support from the ANID Doctoral Fellowship through grant number 21231305. FG gratefully acknowledges support from the French National Research Agency (ANR) funded projects “MWDisc” (ANR-20-CE31-0004) and “Pristine” (ANR-18-CE31-0017). This research made use of the Astropy ([Astropy Collaboration 2013, 2018](#)), Matplotlib ([Hunter 2007](#)) and Numpy ([Harris et al. 2020](#)) packages.

References

- Abadi, M. G., Navarro, J. F., Steinmetz, M., & Eke, V. R. 2003, *ApJ*, 597, 21
 Aguado-Agelet, F., Massari, D., Monelli, M., et al. 2025, *A&A*, 704, A255
 Amarante, J. A. S., Debattista, V. P., Beraldo e Silva, L., Laporte, C. F. P., & Deg, N. 2022, *ApJ*, 937, 12
 Astropy Collaboration (Robitaille, T. P., et al.) 2013, *A&A*, 558, A33
 Astropy Collaboration (Price-Whelan, A. M., et al.) 2018, *AJ*, 156, 123

- Atkinson, K. E. 1991, *An Introduction to Numerical Analysis*, 2nd edn. (John Wiley & Sons)
- Bacon, R., Accardo, M., Adjali, L., et al. 2010, *SPIE Conf. Ser.*, 7735, 773508
- Barbá, R. H., Minniti, D., Geisler, D., et al. 2019, *ApJ*, 870, L24
- Baumgardt, H. 2017, *MNRAS*, 464, 2174
- Baumgardt, H., & Hilker, M. 2018, *MNRAS*, 478, 1520
- Baumgardt, H., & Vasiliev, E. 2021, *MNRAS*, 505, 5957
- Belokurov, V., & Kravtsov, A. 2022, *MNRAS*, 514, 689
- Belokurov, V., & Kravtsov, A. 2024, *MNRAS*, 528, 3198
- Belokurov, V., Erkal, D., Evans, N. W., Koposov, S. E., & Deason, A. J. 2018, *MNRAS*, 478, 611
- Bennett, M., & Bovy, J. 2019, *MNRAS*, 482, 1417
- Bensby, T., Feltzing, S., & Oey, M. S. 2014, *A&A*, 562, A71
- Bica, E., Ortolani, S., Barbuy, B., & Oliveira, R. A. P. 2024, *A&A*, 687, A201
- Binney, J., & Tremaine, S. 2008, *Galactic Dynamics*, 2nd edn. (Princeton University Press)
- Bovy, J. 2015, *ApJS*, 216, 29
- Bullock, J. S., & Johnston, K. V. 2005, *ApJ*, 635, 931
- Callingham, T. M., Cautun, M., Deason, A. J., et al. 2022, *MNRAS*, 513, 4107
- Ceccarelli, E., Massari, D., Mucciarelli, A., et al. 2024, *A&A*, 684, A37
- Ceccarelli, E., Massari, D., Aguado-Agelet, F., et al. 2025, *A&A*, accepted [arXiv:2503.02939]
- Chandrasekhar, S. 1943a, *ApJ*, 97, 255
- Chandrasekhar, S. 1943b, *ApJ*, 97, 263
- Chandrasekhar, S. 1943c, *ApJ*, 98, 54
- Chen, Y., & Gnedin, O. Y. 2024, *Open J. Astrophys.*, 7, 23
- Chiba, R., & Schönrich, R. 2021, *MNRAS*, 505, 2412
- Chiba, R., Friske, J. K. S., & Schönrich, R. 2021, *MNRAS*, 500, 4710
- Dillamore, A. M., & Sanders, J. L. 2025, *MNRAS*, 542, 1331
- Dillamore, A. M., Belokurov, V., & Evans, N. W. 2024, *MNRAS*, 532, 4389
- Dodd, E., Callingham, T. M., Helmi, A., et al. 2022, *VizieR Online Data Catalog: Gaia DR3 of substructure in the stellar halo (Dodd+, 2023)*, *VizieR On-line Data Catalog: J/A+A/670/L2*. Originally published in: 2023A&A...670L...2D
- Dodd, E., Callingham, T. M., Helmi, A., et al. 2023, *A&A*, 670, L2
- Eggen, O. J., Lynden-Bell, D., & Sandage, A. R. 1962, *ApJ*, 136, 748
- Forbes, D. A. 2020, *MNRAS*, 493, 847
- Forbes, D. A., & Bridges, T. 2010, *MNRAS*, 404, 1203
- Gaia Collaboration (Prusti, T., et al.) 2016, *A&A*, 595, A1
- Gaia Collaboration (Vallenari, A., et al.) 2023, *A&A*, 674, A1
- Garro, E. R., Minniti, D., Alessi, B., et al. 2022, *A&A*, 659, A155
- Garro, E. R., Fernández-Trincado, J. G., Minniti, D., et al. 2023, *A&A*, 669, A136
- Gómez, F. A., Helmi, A., Brown, A. G. A., & Li, Y.-S. 2010, *MNRAS*, 408, 935
- Gran, F., Zoccali, M., Saviane, I., et al. 2022, *MNRAS*, 509, 4962
- Gran, F., Kordopatis, G., Zoccali, M., et al. 2024, *A&A*, 683, A167
- GRAVITY Collaboration (Abuter, R., et al.) 2019, *A&A*, 625, L10
- Hairer, E., Lubich, C., & Wanner, G. 2003, *Acta Numerica*, 12, 399
- Harris, C. R., Millman, K. J., van der Walt, S. J., et al. 2020, *Nature*, 585, 357
- Hartke, J., Kakkad, D., Reyes, C., et al. 2020, *SPIE Conf. Ser.*, 11448, 114480V
- Hayden, M. R., Bovy, J., Holtzman, J. A., et al. 2015, *ApJ*, 808, 132
- Haywood, M., Di Matteo, P., Lehnert, M. D., et al. 2018, *ApJ*, 863, 113
- Haywood, M., Khoperskov, S., Cerqui, V., et al. 2024, *A&A*, 690, A147
- Helmi, A., & de Zeeuw, P. T. 2000, *MNRAS*, 319, 657
- Helmi, A., & White, S. D. M. 1999, *MNRAS*, 307, 495
- Helmi, A., White, S. D. M., de Zeeuw, P. T., & Zhao, H. 1999, *Nature*, 402, 53
- Helmi, A., Babusiaux, C., Koppelman, H. H., et al. 2018, *Nature*, 563, 85
- Horta, D., Schiavon, R. P., Mackereth, J. T., et al. 2021, *MNRAS*, 500, 1385
- Horta, D., Schiavon, R. P., Mackereth, J. T., et al. 2023, *MNRAS*, 520, 5671
- Hunter, J. D. 2007, *Comput. Sci. Eng.*, 9, 90
- Ibata, R. A., Gilmore, G., & Irwin, M. J. 1994, *Nature*, 370, 194
- Khoperskov, S., Minchev, I., Libeskind, N., et al. 2023, *A&A*, 677, A90
- Koppelman, H., Helmi, A., & Veljanoski, J. 2018, *ApJ*, 860, L11
- Koppelman, H. H., Helmi, A., Massari, D., Price-Whelan, A. M., & Starkenburg, T. K. 2019a, *A&A*, 631, L9
- Koppelman, H. H., Helmi, A., Massari, D., Roelenga, S., & Bastian, U. 2019b, *A&A*, 625, A5
- Koppelman, H. H., Bos, R. O. Y., & Helmi, A. 2020, *A&A*, 642, L18
- Kruijssen, J. M. D., Pfeffer, J. L., Reina-Campos, M., Crain, R. A., & Bastian, N. 2019, *MNRAS*, 486, 3180
- Kruijssen, J. M. D., Pfeffer, J. L., Chevance, M., et al. 2020, *MNRAS*, 498, 2472
- Leaman, R., VandenBerg, D. A., & Mendel, J. T. 2013, *MNRAS*, 436, 122
- Lian, J., Zasowski, G., Mackereth, T., et al. 2022, *MNRAS*, 513, 4130
- Lim, D., Koch-Hansen, A. J., Chung, C., et al. 2021, *A&A*, 647, A34
- Long, K., & Murali, C. 1992, *ApJ*, 397, 44
- Lövdal, S. S., Ruiz-Lara, T., Koppelman, H. H., et al. 2022, *A&A*, 665, A57
- Mace, G., Sokal, K., Lee, J.-J., et al. 2018, *SPIE Conf. Ser.*, 10702, 107020Q
- Majewski, S. R., Skrutskie, M. F., Weinberg, M. D., & Ostheimer, J. C. 2003, *ApJ*, 599, 1082
- Majewski, S. R., Schiavon, R. P., Frinchaboy, P. M., et al. 2017, *AJ*, 154, 94
- Malhan, K. 2022, *ApJ*, 930, L9
- Malhan, K., & Rix, H.-W. 2024, *ApJ*, 964, 104
- Malhan, K., Ibata, R. A., Sharma, S., et al. 2022, *ApJ*, 926, 107
- Malhan, K., Yuan, Z., Ibata, R. A., et al. 2024, *VizieR Online Data Catalog: Stars of the LMS-1 stream with sp. obs. (Malhan+, 2021)*, *VizieR On-line Data Catalog: J/ApJ/920/51*. Originally published in: 2021ApJ...920...51M
- Marín-Franch, A., Aparicio, A., Piotto, G., et al. 2009, *ApJ*, 694, 1498
- Massari, D. 2025, *RNAAS*, 9, 64
- Massari, D., Koppelman, H. H., & Helmi, A. 2019, *A&A*, 630, L4
- Massari, D., Aguado-Agelet, F., Monelli, M., et al. 2023, *A&A*, 680, A20
- Matsuno, T., Aoki, W., & Suda, T. 2019, *ApJ*, 874, L35
- McKee, C. F., Parravano, A., & Hollenbach, D. J. 2015, *ApJ*, 814, 13
- McMillan, P. J. 2017, *MNRAS*, 465, 76
- Minniti, D., Lucas, P. W., Emerson, J. P., et al. 2010, *New A*, 15, 433
- Minniti, D., Fernández-Trincado, J. G., Smith, L. C., et al. 2021, *A&A*, 648, A86
- Minniti, D., Matsunaga, N., Fernández-Trincado, J. G., et al. 2024, *A&A*, 683, A150
- Miyamoto, M., & Nagai, R. 1975, *PASJ*, 27, 533
- Moni Bidin, C., Mauro, F., Geisler, D., et al. 2011, *A&A*, 535, A33
- Moreno, E., Fernández-Trincado, J. G., Pérez-Villegas, A., Chaves-Velasquez, L., & Schuster, W. J. 2022, *MNRAS*, 510, 5945
- Myeong, G. C., Evans, N. W., Belokurov, V., Sanders, J. L., & Koposov, S. E. 2018, *MNRAS*, 478, 5449
- Myeong, G. C., Vasiliev, E., Iorio, G., Evans, N. W., & Belokurov, V. 2019, *MNRAS*, 488, 1235
- Myeong, G. C., Belokurov, V., Aguado, D. S., et al. 2022, *ApJ*, 938, 21
- Naidu, R. P., Conroy, C., Bonaca, A., et al. 2020, *ApJ*, 901, 48
- Naidu, R. P., Conroy, C., Bonaca, A., et al. 2021, *ApJ*, 923, 92
- Navarro, J. F., Frenk, C. S., & White, S. D. M. 1996, *ApJ*, 462, 563
- Necib, L., Ostdiek, B., Lisanti, M., et al. 2020a, *ApJ*, 903, 25
- Necib, L., Ostdiek, B., Lisanti, M., et al. 2020b, *Nat. Astron.*, 4, 1078
- Necib, L., Ostdiek, B., Lisanti, M., et al. 2022, *Nat. Astron.*, 6, 866
- Newberg, H. J., Yanny, B., & Willett, B. A. 2009, *ApJ*, 700, L61
- Olivares Carvajal, J., Zoccali, M., Rojas-Arriagada, A., et al. 2022, *MNRAS*, 513, 3993
- Olivares Carvajal, J., Zoccali, M., De Leo, M., et al. 2024, *A&A*, 687, A312
- Oria, P.-A., Tenachi, W., Ibata, R., et al. 2022, *ApJ*, 936, L3
- Orkney, M. D. A., Laporte, C. F. P., Grand, R. J. J., et al. 2023, *MNRAS*, 525, 683
- Pagnini, G., Di Matteo, P., Khoperskov, S., et al. 2023, *A&A*, 673, A86
- Park, C., Jaffe, D. T., Yuk, I.-S., et al. 2014, *SPIE Conf. Ser.*, 9147, 91471D
- Peebles, P. J. E. 1965, *ApJ*, 142, 1317
- Peebles, P. J. E., & Yu, J. T. 1970, *ApJ*, 162, 815
- Pérez-Villegas, A., Barbuy, B., Kerber, L. O., et al. 2020, *MNRAS*, 491, 3251
- Plummer, H. C. 1911, *MNRAS*, 71, 460
- Prudil, Z., Kunder, A., Beraldo e Silva, L., et al. 2025, *A&A*, 695, A211
- Queiroz, A. B. A., Chiappini, C., Pérez-Villegas, A., et al. 2021, *A&A*, 656, A156
- Re Fiorentin, P., Spagna, A., Lattanzi, M. G., & Cignoni, M. 2021, *ApJ*, 907, L16
- Re Fiorentin, P., Spagna, A., Lattanzi, M. G., Cignoni, M., & Vitali, S. 2024, *ApJ*, 977, 278
- Read, J. I., Pontzen, A. P., & Viel, M. 2006, *MNRAS*, 371, 885
- Reid, M. J. 2008, in *IAU Symposium, Vol. 248, A Giant Step: from Milli- to Micro-arcsecond Astrometry*, eds. W. J. Jin, I. Platais, & M. A. C. Perryman, 141
- Rix, H.-W., Chandra, V., Andrae, R., et al. 2022, *ApJ*, 941, 45
- Roberts, J. A. G., & Quispel, G. R. W. 1992, *Phys. Rep.*, 216, 63
- Ruchti, G. R., Read, J. I., Feltzing, S., Pipino, A., & Bensby, T. 2014, *MNRAS*, 444, 515
- Ruiz-Lara, T., Matsuno, T., Lövdal, S. S., et al. 2022, *A&A*, 665, A58
- Saito, R. K., Hempel, M., Minniti, D., et al. 2012, *A&A*, 537, A107
- Sanders, J. L., Smith, L., & Evans, N. W. 2019, *MNRAS*, 488, 4552
- Schönrich, R., Binney, J., & Dehnen, W. 2010, *MNRAS*, 403, 1829
- Searle, L., & Zinn, R. 1978, *ApJ*, 225, 357
- Shen, J., & Zheng, X.-W. 2020, *Res. Astron. Astrophys.*, 20, 159
- Shipp, N., Drlica-Wagner, A., Balbinot, E., et al. 2018, *ApJ*, 862, 114
- Shipp, N., Li, T. S., Pace, A. B., et al. 2019, *ApJ*, 885, 3
- Ströbele, S., La Penna, P., Arsenaault, R., et al. 2012, *SPIE Conf. Ser.*, 8447, 844737
- Stuik, R., Bacon, R., Conzelmann, R., et al. 2006, *New A Rev.*, 49, 618
- Sun, G., Wang, Y., Liu, C., et al. 2023, *Res. Astron. Astrophys.*, 23, 015013
- Tenachi, W., Oria, P.-A., Ibata, R., et al. 2022, *ApJ*, 935, L22
- Trick, W. H. 2022, *MNRAS*, 509, 844

- Valenti, E., Zoccali, M., Gonzalez, O. A., et al. 2016, [A&A](#), **587**, L6
- Vasiliev, E. 2019a, [MNRAS](#), **482**, 1525
- Vasiliev, E. 2019b, [MNRAS](#), **484**, 2832
- Vasiliev, E., & Baumgardt, H. 2021, [MNRAS](#), **505**, 5978
- Verlet, L. 1967, [Phys. Rev.](#), **159**, 98
- Wang, S., Necib, L., Ji, A. P., et al. 2023, [ApJ](#), **955**, 129
- Wegg, C., Gerhard, O., & Portail, M. 2015, [MNRAS](#), **450**, 4050
- White, S. D. M., & Rees, M. J. 1978, [MNRAS](#), **183**, 341
- Woudenberg, H. C., & Helmi, A. 2025, [A&A](#), **700**, A240
- Yuan, Z., Smith, M. C., Xue, X.-X., et al. 2019, [ApJ](#), **881**, 164
- Yuan, Z., Chang, J., Beers, T. C., & Huang, Y. 2020, [ApJ](#), **898**, L37
- Yuan, Z., Malhan, K., Sestito, F., et al. 2022, [ApJ](#), **930**, 103
- Zinn, R. 1985, [ApJ](#), **293**, 424
- Zinn, R. 1996, in [Astronomical Society of the Pacific Conference Series](#), 92, Formation of the Galactic Halo...Inside and Out, eds. H. L. Morrison & A. Sarajedini, 211
- Zoccali, M., Valenti, E., & Gonzalez, O. A. 2018, [A&A](#), **618**, A147
- Zoccali, M., Quezada, C., Contreras Ramos, R., et al. 2024, [A&A](#), **689**, A240

Appendix A: Impact of observational errors: worst cases

As mentioned in Sect. 2, we tested that our results (the attribution of each GC to a specific progenitor) are robust even when taking into account observational errors. Here we show the worst cases out of the entire sample, even for them the classification doesn't become ambiguous when taking into account the uncertainties. In Fig. A.1 we show the high energy GCs AM 1 (grey star), Eridanus (blue star), Palomar 3 (red star) and Palomar 4 (orange star), the GCs with the highest distance uncertainties, in the $L_z - L_\perp$ space. The underlying coloured contours in the same tonalities (greys for AM 1, blues for Eridanus, etc...) show the density distribution of 1000 integrations with different input phase space values generated by extracting from the error distributions of each GC. We also show the nearest progenitor families (Sag, HS, the retrogrades, and the other Elqui member). It is clear from the figure that, even for the cases with the largest scatter (AM 1, Palomar 4), accounting for the errors doesn't change the classification of these GCs. Similarly, in Fig. A.2 we show 2MASS-GC01 (red star) and Patchick 122 (green star), the GCs with the highest uncertainties on their velocity vector, in $\varepsilon - Z_{max}$ space. The underlying matching coloured contours show the density distribution of 1000 iterations accounting for the observational errors. As before, we also show the nearest progenitor families (bulge, disc, and low-E) and it appears clear that, even accounting for the errors, the two GCs cannot be identified as anything but disc GCs.

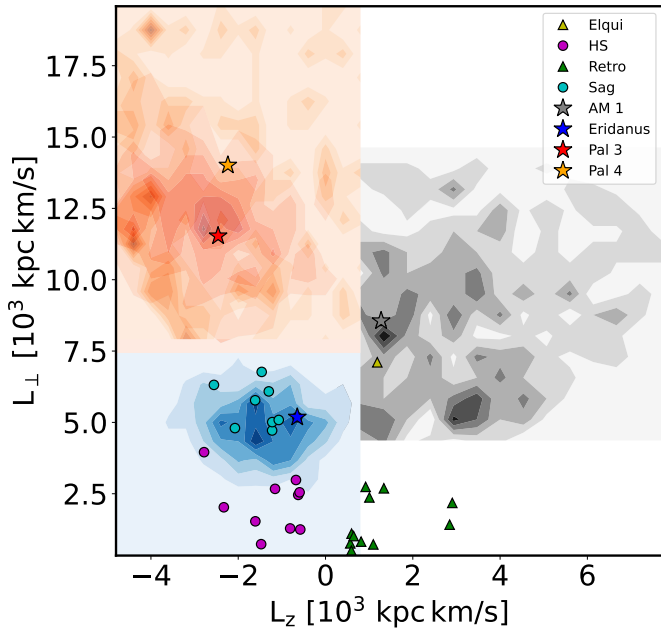


Fig. A.1: $L_z - L_\perp$ space distribution of the GCs with the highest distance uncertainties (filled stars). The underlying matching coloured contours are the distributions of 1000 iterations accounting for the observational errors. The other filled symbols (circles, triangles) are the GCs members of the nearby progenitor families.

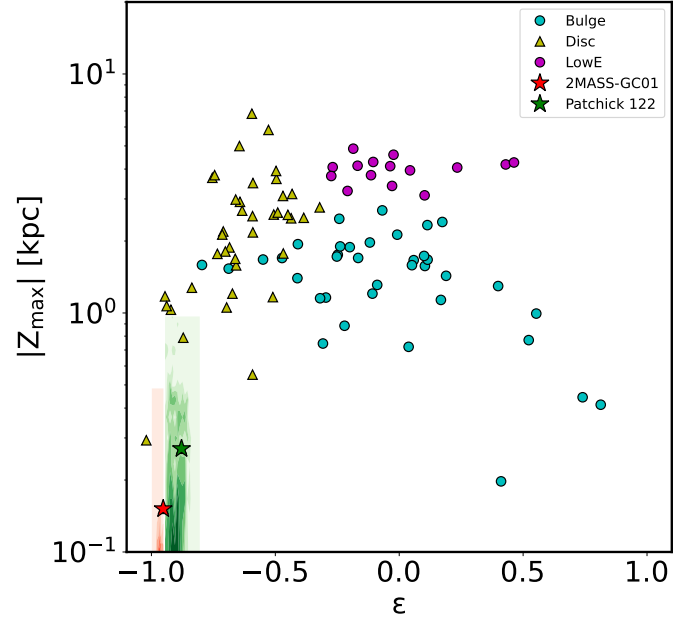


Fig. A.2: $\varepsilon - Z_{max}$ space distribution of the GCs with the highest velocity vector uncertainties (filled stars). The underlying matching coloured contours are the distributions of 1000 iterations accounting for the observational errors. The other filled symbols (circles, triangles) are the GCs members of the nearby progenitor families.

Appendix B: Sanity checks and tests of ORBIT

To ensure that ORBIT works properly we performed an extensive array of tests, both in configurations with a symmetric and static potential (excluding the rotating bar and the central BH) and with the full time-evolving model. In the static and symmetric case, we checked the conservation of the 2 IoMs, the total mechanical energy $E_{tot} = K + U$ and the angular momentum around the symmetry axis, L_z . With the full model, the only surviving IoM is the Jacobi energy (or Jacobi integral Binney & Tremaine 2008), $E_J = E_{tot} - \Omega_b \cdot L$ (where Ω_b is the pattern speed of the rotation and L is the angular momentum corresponding to the axis of rotation, in our case L_z). Fig. B.1 shows the ratios of the variation of the three IoMs during integrations of $5 \cdot 10^6$ steps for a total of 5 Gyr . The ratios are computed as $\Delta X/X_0$ with the variation of each IoM being the value at every step minus the initial value, $\Delta X = X - X_0$ (with X being one of E_{tot} , L_z , E_J).

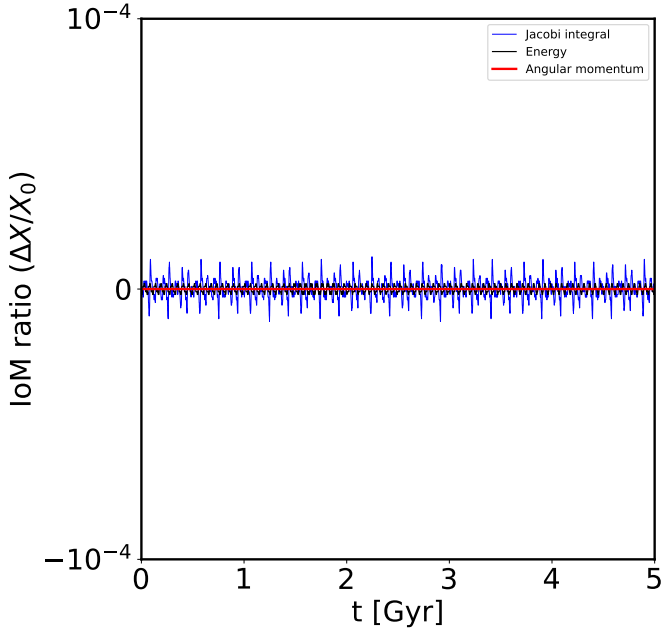


Fig. B.1: Evolution of the IoMs over a typical orbital integration. In black and red, respectively, the total mechanical energy E_{tot} and the angular momentum L_z for the case with a symmetric and static potential. In blue the Jacoby integral E_J for the case with the full potential.

Appendix C: Data table

Table C.1 is an excerpt of the results derived by ORBIT, the full table is only available in electronic form at the CDS.

Table C.1: Recovered orbital parameters, IoMs, adiabatic invariants, and derived quantities used for this analysis for each GC studied. The full table is available at the CDS.

Cluster	R_{peri} [kpc]	R_{apo} [kpc]	ecc	$ Z_{\text{max}} $ [kpc]	E_{tot} [km ² /s ²]	L_z [kpc km/s]	L_{\perp} [kpc km/s]	J_{\parallel}	J_{\perp}	ε
2MASS-GC01	2.54 ± 0.90	4.90 ± 0.21	0.34 ± 0.15	0.15	-148604.9	-924.6027	62.08	-0.96	-0.04	-0.95
2MASS-GC02	1.19 ± 0.59	2.79 ± 0.28	0.43 ± 0.25	1.17	-195646.9	-217.38	84.90	-0.68	-0.22	-0.51
AM 1	38.08 ± 13.46	167.96 ± 59.38	0.84 ± 0.30	110.59	-32665.03	1273.80	8558.58	0.10	0.27	0.10
AM 4	26.45 ± 2.04	37.72 ± 2.91	0.19 ± 0.02	34.41	-59019.18	1034.26	5417.18	0.18	0.77	0.18
Arp 2	21.50 ± 3.63	95.34 ± 16.12	0.74 ± 0.12	78.61	-42849.35	-1611.98	5775.14	-0.19	0.21	-0.17
BH 140	1.87 ± 0.32	11.68 ± 1.00	0.74 ± 0.03	2.65	-118729.4	-721.66	297.19	-0.53	-0.38	-0.45
BH 261	1.69 ± 0.34	2.64 ± 0.23	0.22 ± 0.13	1.05	-183308.9	-372.60	243.23	-0.77	0.07	-0.70
Crater	116.34 ± 67.17	220.74 ± 127.45	0.46 ± 0.27	128.76	-25927.12	5541.70	14870.94	0.31	0.48	0.32
Djor 1	1.31 ± 0.28	8.50 ± 0.73	0.74 ± 0.04	1.60	-133058.6	-544.76	173.68	-0.53	-0.42	-0.44
Djor 2	0.60 ± 0.04	0.78 ± 0.02	0.13 ± 0.04	0.44	-242466.5	129.15	94.67	0.77	0.14	0.74